

# Adaptive Circuit Learning of Born Machine: Towards Realization of Amplitude Embedding and Data Loading

Chun-Tse Li<sup>1,5</sup> and Hao-Chung Cheng<sup>1,2,3,4,5</sup>

<sup>1</sup>*Department of Electrical Engineering and Graduate Institute of*

*Communication Engineering, National Taiwan University, Taipei 106, Taiwan (R.O.C.)*

<sup>2</sup>*Department of Mathematics, National Taiwan University, Taipei 106, Taiwan (R.O.C.)*

<sup>3</sup>*Center for Quantum Science and Engineering, National Taiwan University*

<sup>4</sup>*Physics Division, National Center for Theoretical Sciences, Taipei 10617, Taiwan (R.O.C.) and*

<sup>5</sup>*Hon Hai Quantum Computing Research Center, Taipei, Taiwan*

With the progress in the quantum algorithm in recent years, much of the existing literature claims the exponential quantum advantage against their classical counterpart. However, many of these successes hinge on the assumption that arbitrary states can be efficiently prepared in quantum circuits. In reality, crafting a circuit to prepare a generic  $n$ -qubit quantum state demands an operation count on the order of  $\mathcal{O}(2^n)$ , which is prohibitively demanding for the quantum algorithm to demonstrate its advantage against the classical one. To tackle this data-loading problem, numerous strategies have been put forward. Nonetheless, most of these approaches only consider a very simple and easy-to-implement circuit structure, which has been shown to suffer from serious optimization issues.

In this study, we harness quantum circuits as Born machines to generate probability distributions. Drawing inspiration from methods used to investigate electronic structures in quantum chemistry and condensed matter physics, we present a novel algorithm "Adaptive Circuit Learning of Born Machine" (ACLBM) that dynamically expands the ansatz circuit. Our algorithm is tailored to selectively integrate two-qubit entangled gates that best capture the complex entanglement present within the target state. Empirical results underscore the proficiency of our approach in encoding real-world data through amplitude embedding, demonstrating not only compliance with but also enhancement over the performance benchmarks set by previous research.

## I. INTRODUCTION

Over the past two decades, intensive research within the quantum computing community has spurred rapid advancements in quantum algorithms, yielding promising applications across diverse fields of study. These include solving systems of linear equations [1–4], Hamiltonian simulation [5–10], the Quantum Approximation Optimization Algorithm [11–13], quantum walks [14, 15], Quantum Principal Component Analysis [16], and Quantum Support Vector Machines [17]. However, many of these quantum algorithms' claims of exponential speedup over their classical counterparts are contingent upon the assumption that arbitrary quantum states can be efficiently prepared. In reality, studies have shown that preparing generic quantum states requires either  $\mathcal{O}(2^n/n)$  circuit depth with  $n$  qubits [18–21] or  $\Theta(n)$  circuit depth with  $\mathcal{O}(2^n)$  ancillary qubits [22–24]. Only certain  $d$ -sparse quantum states can be prepared in  $\Theta(\log(nd))$  circuit depth, though this still necessitates  $\mathcal{O}(nd \log(d))$  ancillary qubits [24].

Despite the formidable complexity of state preparation, it remains an open question whether some highly structured quantum states can be approximately constructed with  $\mathcal{O}(\text{poly}(n))$  overhead. To address this, several hybrid quantum-classical algorithms have been proposed. Quantum Generative Adversarial Network (QGAN) [25–27] employ adversarial training to minimize the distance between the distribution produced by a quantum generator and the target distribution. Quan-

tum Circuit Born Machine (QCBM) [28] utilizes the squared maximum mean discrepancy (MMD) loss to assess the distance between the model and target distribution in the kernel feature space, and they construct the entanglement layer based on the Chow-Liu tree [29]. Data Driven Quantum Circuit Learning (DDQCL) [30] applies negative log likelihood as a loss function to train the quantum generator.

While these approaches have showcased promising results in numerical experiments on simpler datasets and therefore claimed their scalability for larger qubit applications, numerical experiments reveal their inability to deliver satisfactory outcomes on more intricate and extensive datasets. The noticeable decline in performance with an increasing problem size can likely be traced back to the simplistic circuit structure initially devised for addressing ground state issues in small molecules [31]. This structure, while straightforward to implement and agnostic to the specific problem, faces substantial optimization challenges. This issue, commonly referred to as barren plateaus, is characterized by a significant reduction in gradient magnitude as the number of qubits increases and the circuit depth grows, leading to an exponential decrease in the gradient [32]. Furthermore, the absence of a data-driven approach in the circuit design process leads to concerns regarding the efficient use of two-qubit gates. The current methodology applies a uniform circuit structure, irrespective of the specific entanglement characteristics of the state being prepared. This one-size-fits-all strategy may not be necessary, particularly for states

that exhibit only weak entanglement. Consequently, the indiscriminate use of a linear structure of two-qubit entangled layers across all qubits could be considered an inefficient allocation of quantum resources.

Conversely, the adaptive circuit structure ansatz, and in particular, the ADAPT-VQE method, as outlined in [33, 34], has attracted considerable interest from the quantum computing community. The ADAPT-VQE iteratively builds the ansatz by selectively incorporating operators, which function as generators of unitary transformations, from a predetermined operator pool based on their gradient magnitudes. This innovative strategy results in the creation of remarkably compact ansatz, delivering superior precision when compared to previous methodologies referenced in [35–37]. Additionally, numerical evidence indicates that ansatz produced by this algorithm are resistant to barren plateaus, offering a more favorable scenario for optimization tasks. Recently, there are some similar algorithms that have been proposed to tackle other challenges, such as quantum machine learning [38] and quantum circuit compilation [39, 40]. However, it is unclear whether adaptive circuit learning can be effectively applied to quantum data loading.

In this study, we embrace the principles of the adaptive circuit learning framework and introduce an algorithm "Adaptive Circuit Learning of Born Machine" (ACLBM) designed to iteratively build an ansatz circuit that is uniquely suited to the problem, while also being compact and efficient in terms of parameters. We extensively benchmark the performance of our model against a variety of datasets, as well as compare it with existing approaches in the literature. Specifically, we focus on representing real-world datasets, such as image data, utilizing the amplitude embedding method. This method involves encoding the image information into the  $2^n$  amplitudes of an  $n$ -qubit state. Our numerical experiments reveal that our method surpasses current techniques [27, 28, 30] by requiring fewer parameters and yielding more accurate results, showcasing an exceptional capability to discern the intrinsic correlations within image data with a parameter count of only  $\mathcal{O}(\text{poly}(n))$ .

## II. RESULTS

### A. Problem formulation

For a generic probability distribution, we construct the dataset  $\mathcal{D} = \{x^1, \dots, x^N\}$  with samples drawn independently and identically distributed (*i.i.d.*) from an unknown distribution  $p_d(x)$ . We then use this dataset to empirically reconstruct an approximated probability mass function (PMF) through the following equation:

$$p(x) = \frac{1}{N} \sum_i \mathbb{1}\{x^i = x\} \approx p_d(x), \quad (1)$$

where  $\mathbb{1}\{x^i = x\}$  is an indicator function. While for real-world datasets, such as images or time-sequential signals, we directly flatten them into one-dimensional vectors (if necessary) and normalize them to conform to a probability distribution  $p(x)$ .

Given the target distribution  $p(x)$ , we aim to recover the state in the following form:

$$|\Psi^*\rangle = \sum_x \sqrt{p(x)}|x\rangle, \quad (2)$$

so that, according to the Born rule, the probability of measuring a specific computational basis  $\{|x\rangle\}_x$  is

$$|\langle x|\Psi^*\rangle|^2 = p(x). \quad (3)$$

Our objective is to find a unitary  $U(\theta)$  that can well recover the target probability distribution when we measure on the computational basis,

$$\text{Tr}(|x\rangle\langle x|U(\theta)|0\rangle\langle 0|^{\otimes n}U^\dagger(\theta)) = q_\theta(x) \approx p(x). \quad (4)$$

### B. Loss criterion

In generative learning, the Kullback–Leibler (KL) divergence is a standard metric for measuring the discrepancy between two probability distributions. It is defined as:

$$\mathcal{L}(\theta) = D_{\text{KL}}(p||q_\theta) = \sum_x p(x) \log \frac{p(x)}{q_\theta(x)}. \quad (5)$$

Numerically, the KL divergence effectively characterizes the distance between distributions across any dimensionality without suffering from diminishing values as the problem size increases.

### C. Adaptive circuit learning algorithm

In this section, we describe the steps of the adaptive circuit learning algorithm in detail. Readers are referred to Fig. 1 for a schematic workflow.

**Operator pool.** The first step in the adaptive circuit learning algorithm is to establish a self-defined operator pool. Grimsley et al.'s foundational ADAPT-VQE work [33] chooses a pool comprising fermionic single and double excitation operators, drawing from the UCC ansatz [36]. This method capitalizes on unitary coupled cluster theory, integrating physical intuition into the operator selection process. However, our problem's context lacks such physical motivations for constructing the operator pool, prompting a shift towards alternative methodologies. The qubit-ADAPT-VQE, proposed by Tang et al. [34], presents a more fitting approach for our scenario. Tang et al. [34] have demonstrated that a pool with a

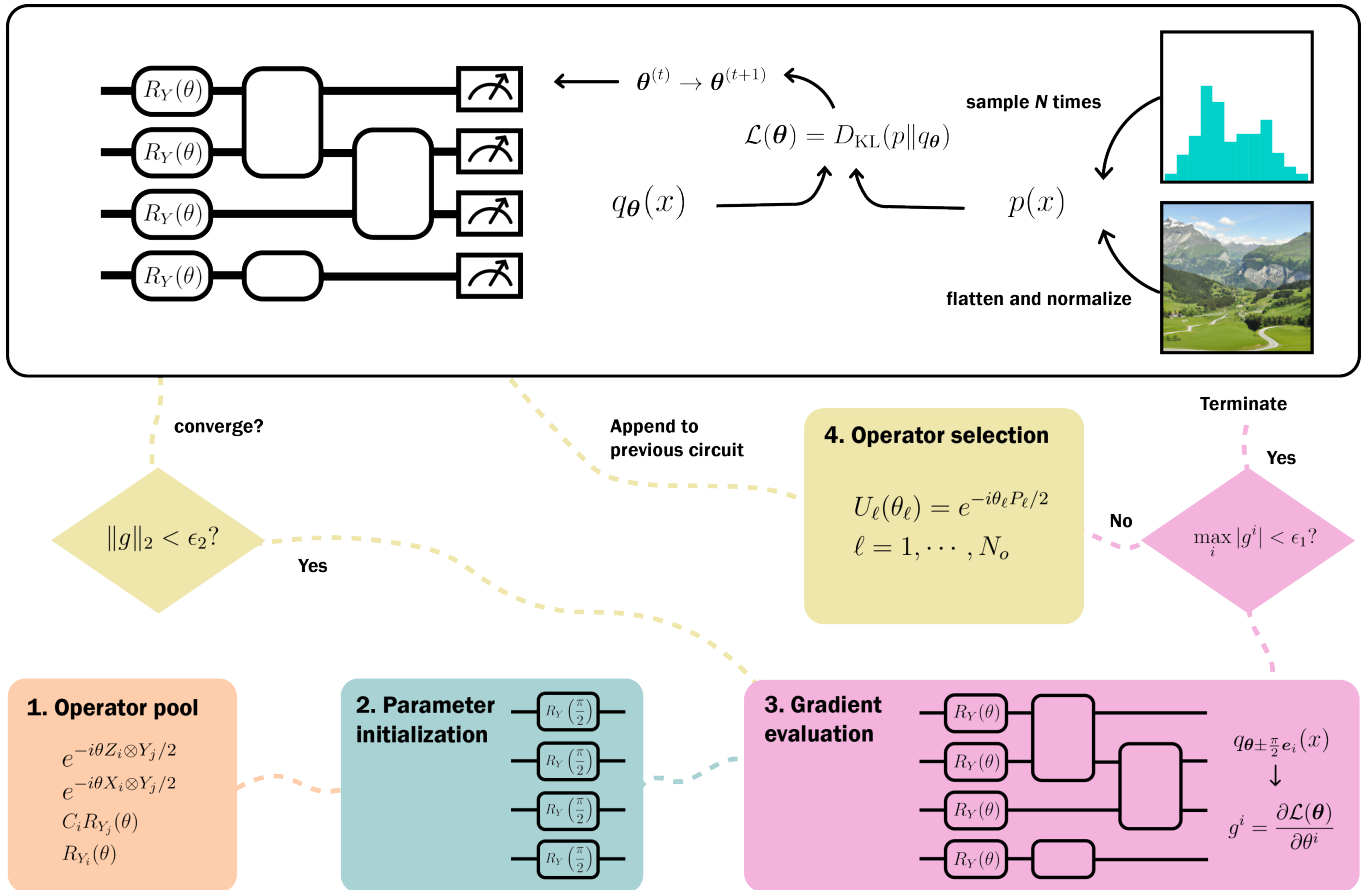


**FIG. 1:** Graphical illustration of the Adaptive Circuit Learning of Born Machine (ACLBM) process. The upper portion of the diagram outlines the quantum data loading framework, where a quantum circuit, functioning as a Born machine, generates a probability distribution. This distribution is then utilized to compute the Kullback-Leibler (KL) divergence, serving as the loss function, which is subsequently minimized by a classical optimizer to update the circuit parameters. The lower portion delineates the adaptive learning workflow. At each epoch, a set of  $N_o$  operators is selected and incorporated into the current circuit configuration. A reoptimization of all parameters follows. The optimization cycle concludes once the convergence criterion – specifically, when the  $L_2$  norm of the gradient vector  $\|g\|_2$  – is less than  $\epsilon_2$ . The entire procedure terminates when the maximum gradient among the selected operators is below  $\epsilon_1$ , ensuring the algorithm’s progression towards a precise solution without perturbing the state, as gradients are evaluated at  $\theta_i = 0$ .

minimal number of  $2n - 2$  operators is complete, capable of generating any arbitrary quantum state. Despite this, our numerical simulations reveal that the exact pool of  $2n - 2$  operators suggested in [34] does not consistently yield satisfactory results. We surmise that this might be attributed to the fact that nearest-neighbor unitary operations struggle to effectively propagate interactions between distant qubits as the problem size increases. To address this, we have expanded their operator pool to encompass any pairs of qubits, specifically focusing on unitary operators with matrix elements that are solely real.

$$e^{-i\theta Z_i \otimes Y_j / 2} = \begin{pmatrix} \cos \frac{\theta}{2} & -\sin \frac{\theta}{2} & 0 & 0 \\ \sin \frac{\theta}{2} & \cos \frac{\theta}{2} & 0 & 0 \\ 0 & 0 & \cos \frac{\theta}{2} & \sin \frac{\theta}{2} \\ 0 & 0 & -\sin \frac{\theta}{2} & \cos \frac{\theta}{2} \end{pmatrix} \quad \forall i \neq j,$$

$$e^{-i\theta X_i \otimes Y_j / 2} = \begin{pmatrix} \cos \frac{\theta}{2} & 0 & 0 & -\sin \frac{\theta}{2} \\ 0 & \cos \frac{\theta}{2} & \sin \frac{\theta}{2} & 0 \\ 0 & -\sin \frac{\theta}{2} & \cos \frac{\theta}{2} & 0 \\ \sin \frac{\theta}{2} & 0 & 0 & \cos \frac{\theta}{2} \end{pmatrix} \quad \forall i \neq j,$$

$$C_i R_{Y_j}(\theta) = \begin{pmatrix} 1 & 0 & 0 & 0 \\ 0 & 1 & 0 & 0 \\ 0 & 0 & \cos \frac{\theta}{2} & -\sin \frac{\theta}{2} \\ 0 & 0 & \sin \frac{\theta}{2} & \cos \frac{\theta}{2} \end{pmatrix} \quad \forall i \neq j,$$

$$R_{Y_i}(\theta) = \begin{pmatrix} \cos \frac{\theta}{2} & -\sin \frac{\theta}{2} \\ \sin \frac{\theta}{2} & \cos \frac{\theta}{2} \end{pmatrix} \quad \forall i. \quad (6)$$

We have selected the real unitary approach, a decision grounded in the observation that when the generator is real (take  $Z_i X_j$  as an example), constraining our state to be real results in a zero gradient. For a comprehensive

proof of this, please refer to Appendix. B.

**Ansatz initialization.** As we can see in the previous section, the majority of the loss functions presented involve the model probability in the denominator. This can potentially result in an explosion of values for both the loss function and its gradient, posing a significant challenge during optimization. To circumvent this issue, we initialize our quantum state to be an equal superposition, achieved by applying a set of  $R_Y(\theta)|_{\theta=\frac{\pi}{2}}$  gates to each qubit. Furthermore, we allow these initial parameters to be trainable in the subsequent optimization phase.

**Gradient evaluation.** In the second step, we compute the gradient of the operator within the pool. Previous studies [34, 36] have demonstrated that the gradient can be derived using the commutation relationship between the Hamiltonian  $H$  and the generator  $P_i$ :

$$\left. \frac{\partial \langle H \rangle_{\theta}}{\partial \theta^i} \right|_{\theta^i=0} = -\frac{i}{2} \langle \psi(\theta) | [H, P_i] | \psi(\theta) \rangle. \quad (7)$$

However, in our case, we do not possess a defined Hamiltonian. As detailed in Appendix. A, we establish that the gradient can be precisely calculated using the parameter-shift rule [41, 42]. This allows us to append the unitary directly to the circuit and utilize three quantum evaluations to compute the exact gradient:

$$\frac{\partial \mathcal{L}(\theta)}{\partial \theta^i} = -\sum_x \frac{p(x)}{q_{\theta}(x)} \left( q_{\theta+\frac{\pi}{2}e_i}(x) - q_{\theta-\frac{\pi}{2}e_i}(x) \right). \quad (8)$$

Notice that if the largest gradient is less than the threshold, say,  $\epsilon_1$  we simply terminate our algorithm.

**Operator selection.** Upon calculating the gradients for each operator, we proceed to choose the top  $N_o$  operators based on their gradient magnitudes. While previous literature, such as the works by Romero et al. [36] and Tang et al. [34], has typically set  $N_o$  to 1, our numerical experiments indicate that a moderately larger  $N_o$  often enhances performance. This approach not only yields better results but also reduces the necessity of repeatedly evaluating the gradients within the operator pool. Additionally, in scenarios involving extremely sparse distributions, a larger  $N_o$  becomes crucial to ensure convergence of the algorithm.

**Optimization.** We incorporate the chosen operator into our ansatz and proceed to optimize all the parameters until convergence is achieved. The convergence criterion is defined as the gradient norm  $\|\mathbf{g}\|_2$  falling below a specified threshold  $\epsilon_2$ .

### III. NUMERICAL EXPERIMENTS

In this section, we present an extensive study through numerical simulations conducted on various datasets. To ensure a fair comparison, we have adhered closely to the experimental settings outlined in the original works [27, 28, 30], with minor modifications to the circuit architecture to enhance performance. The circuit architecture for comparative models incorporates a sequence of  $k+1$  layers of single qubit rotation  $R_X(\theta_{i,1})R_Y(\theta_{i,2})R_X(\theta_{i,3})$  alternated with  $k$  layers of entanglement layer. For the Quantum Circuit Born Machine (QCBM) [28], the entanglement layers are structured based on the Chow-Liu Tree [29]. In contrast, the entanglement strategy for Quantum Generative Adversarial Networks (QGAN) [27] and Data-Driven Quantum Circuit Learning (DDQCL) [30] involves a simpler arrangement where controlled-Z (CZ) gates connect each qubit  $i$  with its neighbor  $(i+1) \bmod n$ . We use ADAM optimizer [43], commonly used in the deep learning community, to optimize the model. In order to rule out the detrimental effect on the finite shot noise, which could obscure the true performance of different models, all experiments are conducted under the assumption that the exact probability distribution of the model,  $q_{\theta}(x)$ , is precisely calculable. This is equivalent to performing an infinite number of measurements. For each experiment, we conducted 20 independent trials and selected the best result for inclusion in our plots. All implementations were carried out using PennyLane [44], interfaced with PyTorch [45].

#### A. Generic probability distribution

We commenced our evaluation with an assessment of our algorithm on a range of generic probability distributions, which were initially utilized as benchmarks in works by Benedetti et al. [30] and Liu et al. [28]. It is noteworthy that these distributions are highly structured and can be specified by a limited number of parameters; consequently, it remains unclear whether there are any efficient techniques specifically tailored for preparing these distributions.

Our analysis focuses on a 10-qubit dataset, examining a log-normal distribution with parameters  $\mu = 5.5, \sigma = 0.9$ , a bimodal distribution with  $\sigma_1 = \sigma_2 = 128, \mu_1 = \frac{2}{7} \cdot 1024, \mu_2 = \frac{5}{7} \cdot 1024$ , and a triangular distribution with a lower limit  $l = 0$ , upper limit  $u = 1023$  and mode  $m = 256$ . For the benchmark models, the number of circuit layers is set to  $k = 10$ , with a total of 330 parameters. As for our model, the number of operators is set to  $N_o = 3$ . Our numerical simulations suggest that while each model can accurately prepare quantum states in datasets with a lower number of qubits, their performance significantly weakens as the problem scale increases. In contrast, our model (ACLBM) exhibits robustness, consistently achieving an excellent fit with the target distribution. The detailed comparison is shown in

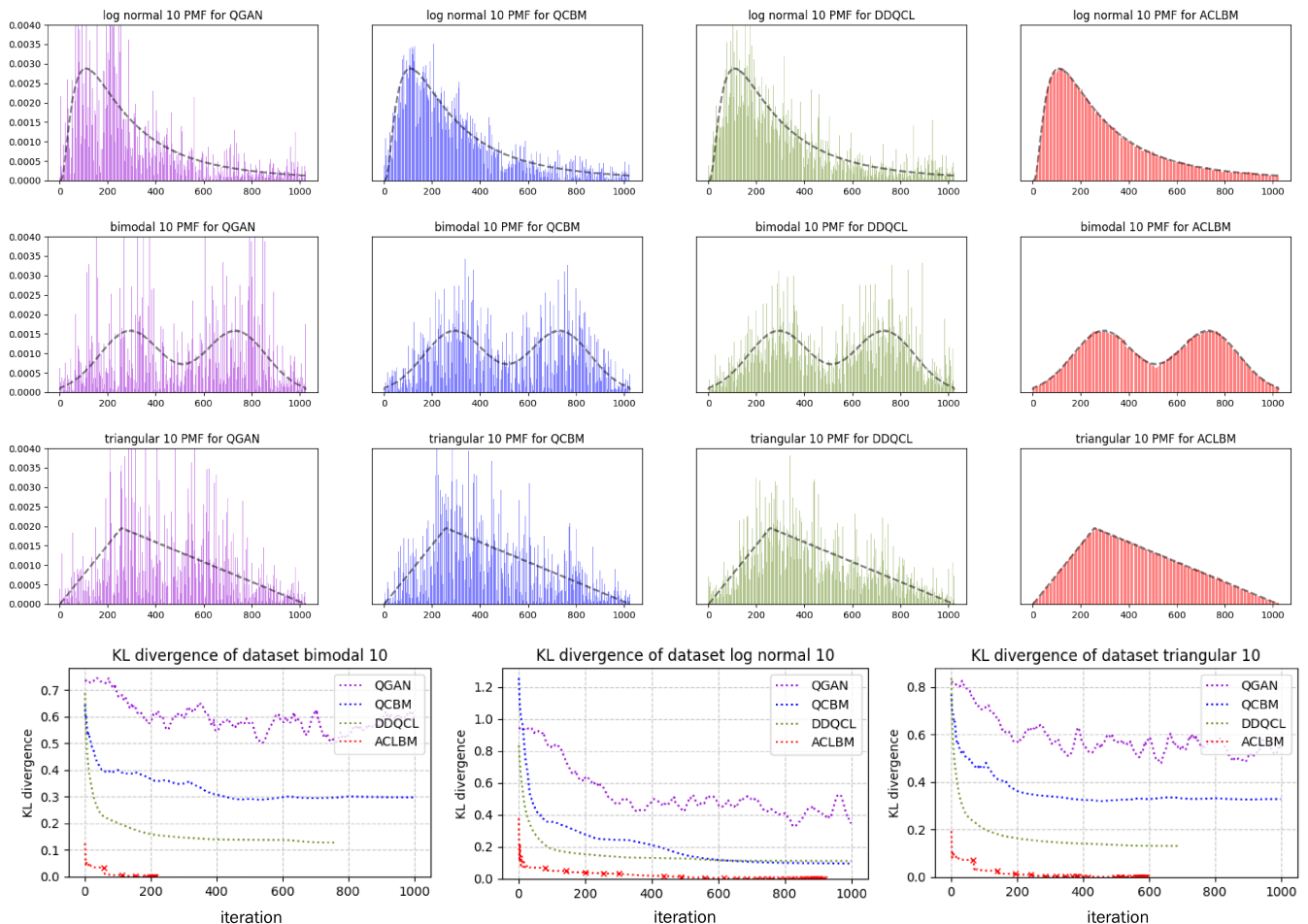


**FIG. 2:** Benchmark comparisons for the generic probability distribution across different models. This figure illustrates the benchmarking of various quantum generative models, with QGAN [27] (purple), QCBM [28] (blue), DDQCL [30] (green), and the proposed ACLBM (red). The top row represents the results for the log-normal distribution, followed by the bimodal distribution in the second row, and the triangular distribution in the third. The bottom row charts the KL divergence over the number of epochs. Benchmark models employ circuits with 10 layers, totaling 330 parameters. In contrast, the proposed ACLBM model demonstrates superior accuracy as well as parameter efficiency with only 93, 45, and 87 parameters for the respective distributions.

Fig. 2.

## B. Bars and Stripes

The Bars and Stripes (BAS) dataset [30, 46, 47] is a set of binary images that are foundational for benchmarking generative models in both classical deep learning and quantum machine learning. Images in BAS display unique patterns of horizontal bars or vertical stripes within a grid, with ‘on’ pixels (1’s) forming the bars or stripes and ‘off’ pixels (0’s) as the background. Due to its binary and combinatorial nature, the BAS dataset serves as a prime candidate for evaluating the ability of generative algorithms to learn and replicate distinct, structured patterns, thus providing insight into the learning model’s capabilities to capture data distributions effectively. All

patterns of BAS  $4 \times 4$  dataset is shown in Fig. 4.

The BAS datasets serve as an excellent testing ground for the entangling capabilities of quantum circuits. This is because finding a close approximation of BAS distributions is nearly impossible using only product states. Our model reflects this challenge; in each epoch, a higher number of operators must be selected to ensure satisfactory convergence.

In our investigation, we examine the  $2 \times 2$ ,  $3 \times 3$ , and  $4 \times 4$  configurations of the BAS dataset, which correspond to quantum problems involving 4, 9, and 16 qubits, respectively. For the comparative benchmark models, the quantum circuit depth is set with  $k = 4$  layers for the  $2 \times 2$  case,  $k = 10$  for the  $3 \times 3$  case, and  $k = 20$  for the  $4 \times 4$  case. The total number of adjustable parameters for these configurations is 60, 297, and 1008, respectively. In contrast, ACLBM employs a variable number of op-

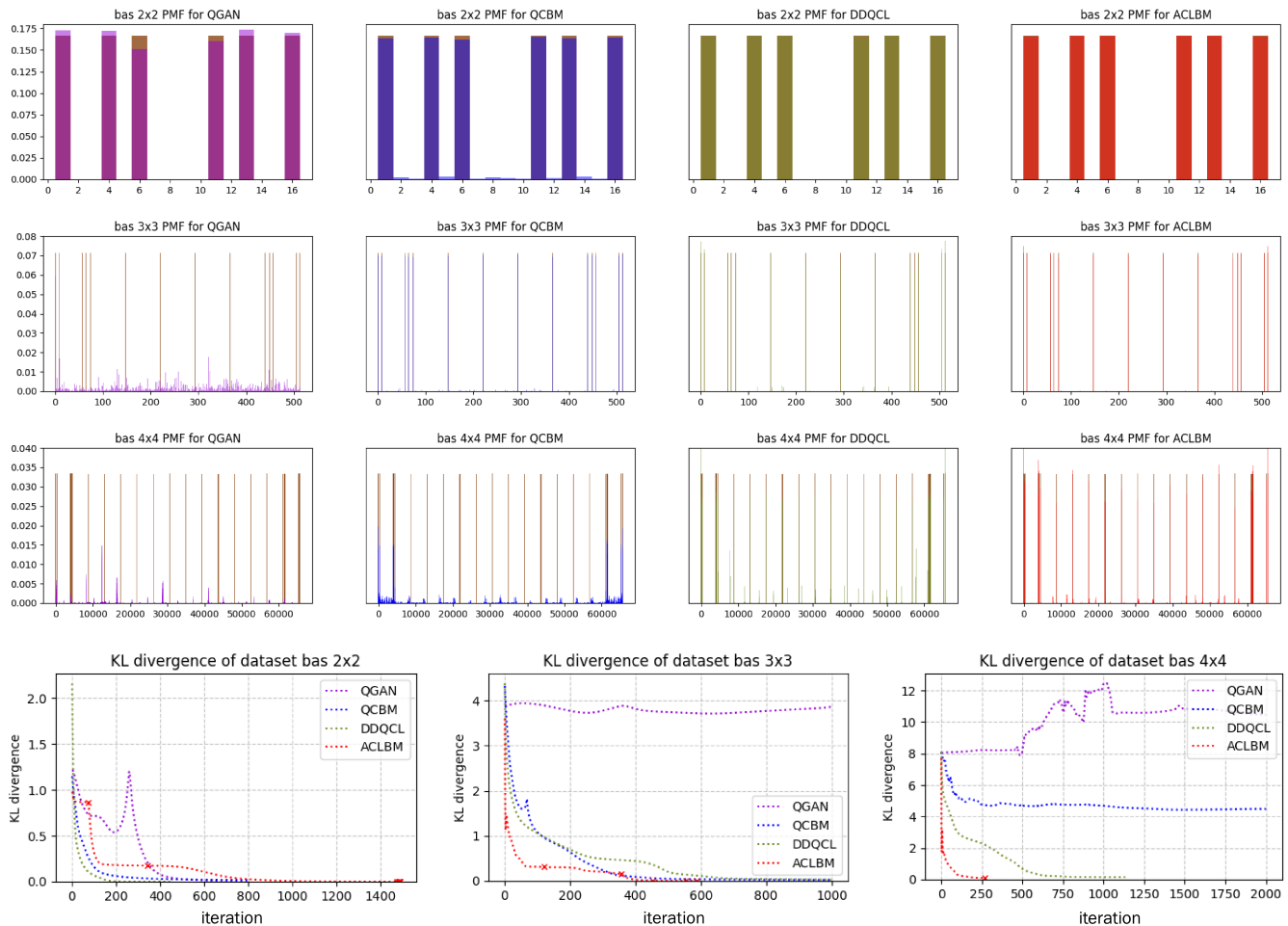


**FIG. 3:** Benchmark comparisons on the Bars and Stripes (BAS) dataset. From top to bottom rows, we present BAS  $2 \times 2$ , BAS  $3 \times 3$ , BAS  $4 \times 4$ , and the KL-divergence respectively. For the  $2 \times 2$  BAS dataset, almost all models can perfectly fit the distribution. However, in the  $3 \times 3$  BAS, the performance of QGAN [27] begins to deteriorate as adversarial training fails to capture the features of the 9-qubit data. In the  $4 \times 4$  BAS, QCBM [28] also suffers from optimization issues, failing to approximate the distribution accurately. In contrast, our model, ACLBM, maintains robustness and exhibits a very fast convergence rate, even with data comprising 65,536 dimensions.



**FIG. 4:** Representative patterns from the  $4 \times 4$  Bars and Stripes (BAS) dataset. This subset includes all permissible configurations of horizontal bars and vertical stripes. Among the  $2^{16} = 65536$  possible patterns for a  $4 \times 4$  grid, only 30 constitute valid BAS patterns.

erators, selecting  $N_o = 3$  for the  $2 \times 2$  case,  $N_o = 45$  for the  $3 \times 3$  case, and  $N_o = 300$  for the  $4 \times 4$  case in each optimization epoch.

Our numerical experiments given in Fig. 3, indicate QCBM [28], DDQCL [30], and ACLBM are all capable

of finding a robust approximation of the BAS distribution, showing consistency across different experimental trials. On the other hand, QGAN [27] exhibits challenges in approximating the distribution when scaling to larger problem sizes, frequently converging to random quantum states rather than the intended distribution. This phenomenon underscores the inherent difficulties and instabilities associated with generative learning, which often requires meticulous selection of hyperparameters and strategic initializations to achieve robustness across varying trials.

### C. Real images

We demonstrate ACLBM's capability for realizing amplitude embedding, a crucial task in quantum machine learning, where image datasets are encoded into the  $2^n$

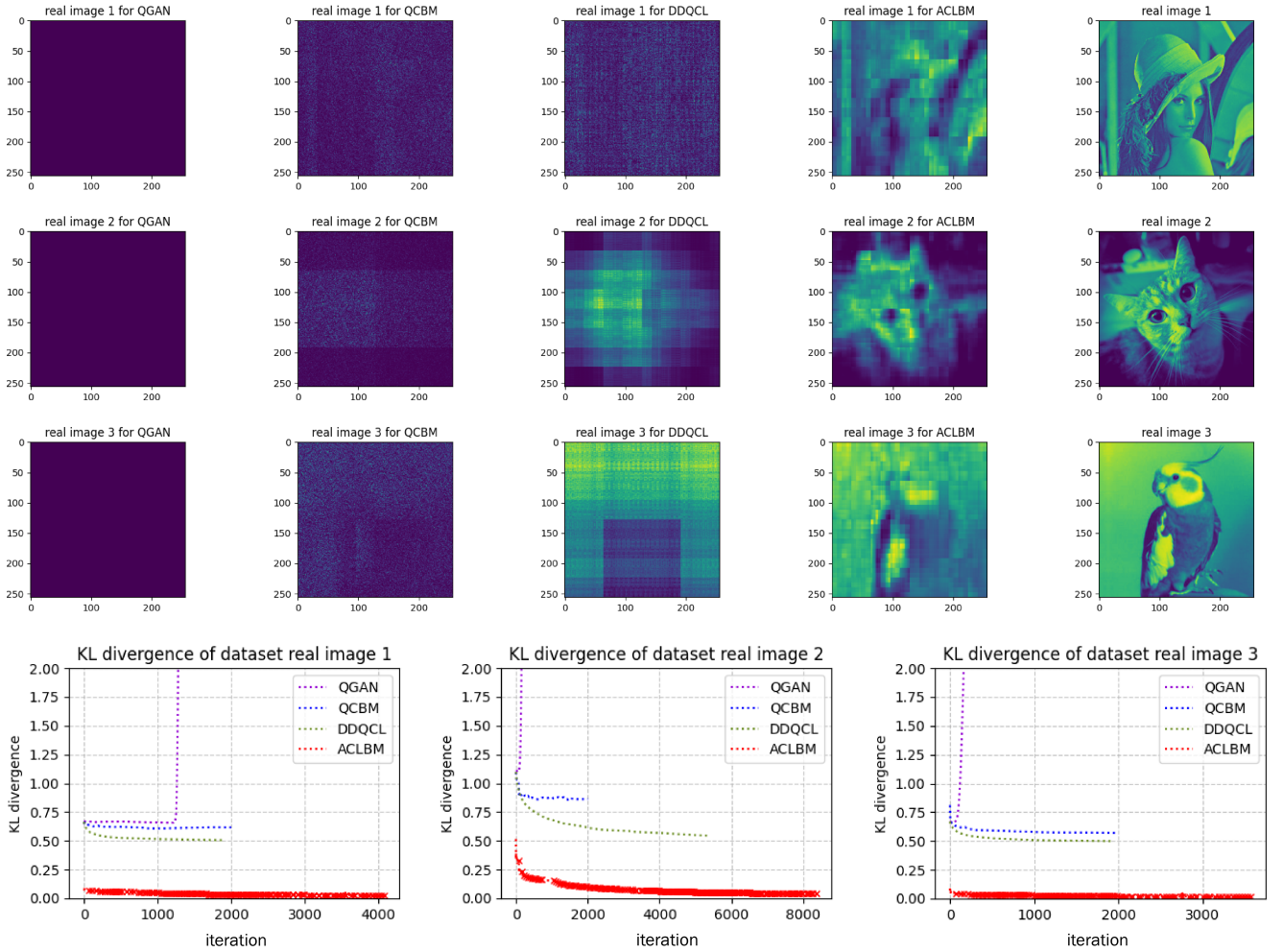


**FIG. 5:** Benchmark comparisons on the real image dataset. For QGAN [27], QCBM [28], and DDQCL [30], we terminate the optimization loop if the gradient norm falls below  $10^{-3}$ . For our model, we set the threshold at  $5 \times 10^{-3}$ . From the figure, it is evident that only our model (ACLBM) captures features recognizable visually, while the other three models do not. We observe that QGAN suffers from catastrophic optimization issues; the losses of the generator and discriminator are extremely unstable, causing the KL divergence to increase as the iteration proceeds.

amplitudes of quantum states. In contrast to previously considered distributions that are defined by a limited number of parameters or are sparse relative to the total dimensionality, image datasets intrinsically present a greater challenge for quantum representation due to their encoding of exponentially more information.

We evaluate three  $256 \times 256$  pixel images, corresponding to a 16-qubit system. These images are flattened into 65536-dimensional vectors and normalized to our target distribution  $\{p(x)\}_{x=0}^{65535}$ . For benchmark models, we set the circuit depth to  $k = 20$  layers, entailing a total of 1,008 parameters. In our approach,  $N_o = 3$  generators are selected in each epoch for circuit construction.

Numerical experiments given in Fig. 5 reveal that, with the exception of our model, other approaches fail to capture the distribution of real-image datasets, resulting in outputs that are indistinguishable to the human eye. In contrast, although the images generated by our model

are somewhat blurred, they retain identifiable features that can be recognized visually. These results manifest the significance of a well-tailored circuit design for accurately approximating complex distributions in quantum machine learning.

It is important to note that the Maximum Mean Discrepancy (MMD) loss function employed by the QCBM [28] is less effective as a loss criterion for larger datasets. While it can measure distribution differences in smaller-scale problems effectively, the MMD loss does not adequately reflect discrepancies in image datasets. As indicated in Table I, a low MMD value does not necessarily correlate with an accurate approximation of the target distribution, often leading to a misleading representation of model performance.

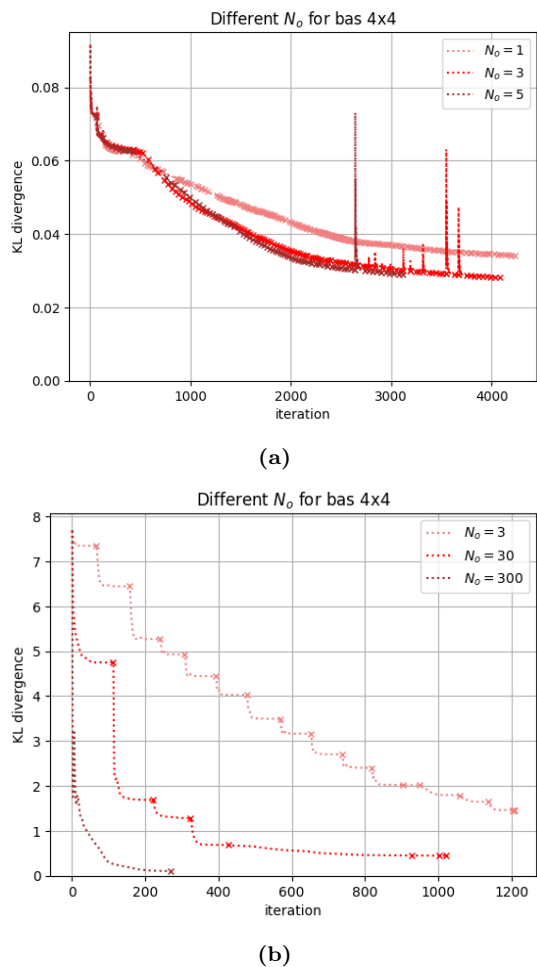


**FIG. 6:** The effect of varying the number of operators,  $N_o$ , on the performance of ACLBM with different datasets. (a) For the densely populated real image 1 dataset, a higher  $N_o$  leads to faster convergence with fewer epochs required: 250 epochs for  $N_o = 1$ , 145 for  $N_o = 3$ , and 85 for  $N_o = 5$ , while using 250, 435, and 425 parameters, respectively. (b) For the sparser BAS  $4 \times 4$  dataset, the number of epochs to convergence decreases significantly with an increase in  $N_o$ : 18 epochs for  $N_o = 3$ , 7 for  $N_o = 30$ , and only 1 for  $N_o = 300$ , corresponding to a parameter count of 54, 210, and 300, respectively.

## D. Discussions

### Number of operators.

We explore the impact of varying the number of operators,  $N_o$ , per epoch on the performance of the Adaptive Circuit Learning of Born Machine (ACLBM). As illustrated in Fig. 6, when applied to a dense distribution (specifically, the real image 1 dataset in our study), a moderate increase in  $N_o$  above 1 slightly enhances both performance and convergence rate. Notably, performance appears to saturate at  $N_o = 3$ . While the  $N_o = 5$  setting achieves faster convergence and requires fewer parameters than the  $N_o = 3$  scenario, the overall

converged KL divergence for these two settings is comparable. In the case of sparse distributions, exemplified by the BAS  $4 \times 4$  dataset, a larger  $N_o$  is essential to ensure convergence. With  $N_o = 3$ , convergence is notably sluggish, and the final KL divergence hovers around 1.5. However, as  $N_o$  increases to 30 or even 300, we see a marked acceleration in convergence and an improved KL divergence. This effect likely stems from the BAS dataset’s inherent need for long-range entanglement, where a smaller  $N_o$  provides insufficient entanglement range, leading to subpar distribution approximation.

### Adjustable learning rate.

To ensure stability and rapid convergence of our model, we adopt an adjustable learning rate, reassigning it a new value at the start of each epoch. This approach prevents the loss function from fluctuating, which commonly occurs when a constant learning rate is too high near convergence. Specifically, we base our learning rate on the norm of the gradient of selected operators, setting it as follows:

$$\text{lr} = \alpha \cdot \frac{\|\mathbf{g}\|_2}{\sqrt{N_o}}. \quad (9)$$

Here,  $\alpha$  is a scaling factor, generally chosen between 0.1 to 0.5, and  $\|\mathbf{g}\|_2$  is the 2-norm of the gradient vector  $\mathbf{g}$ . This strategy allows the learning rate to adapt dynamically, promoting fast and stable convergence.

### Operator Pool Reduction.

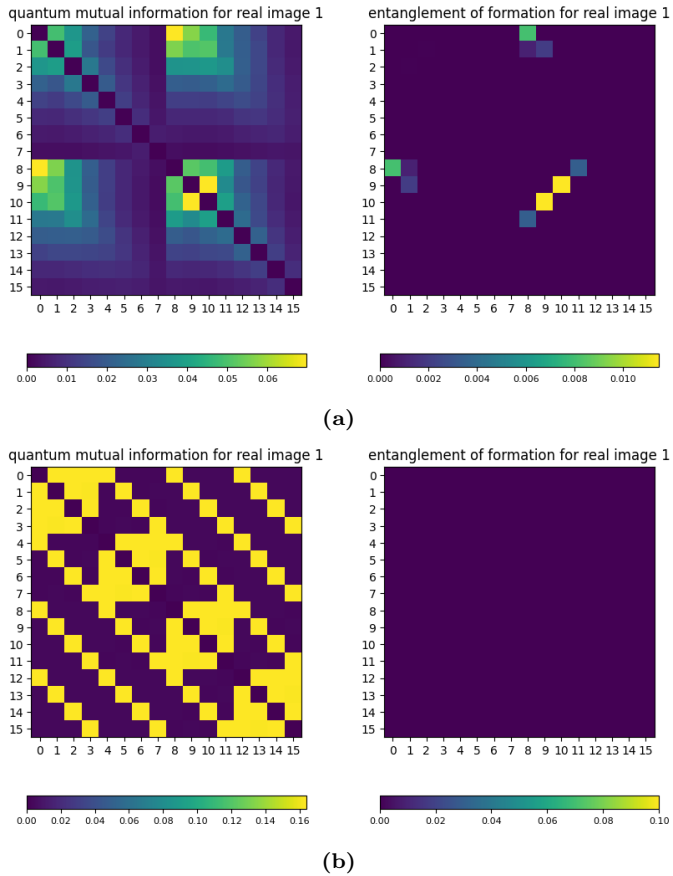
Our algorithm, as it currently stands, evaluates the gradients of  $\mathcal{O}(n^2)$  operators at each epoch. Yet, in certain distributions, specific qubit pairs may contribute more significantly to the overall quantum correlation than others. In such cases, we can streamline the operator pool by retaining only those operators that act on highly correlated qubit pairs, thereby eliminating the less contributory ones. There are numerous methods to assess the correlation between two qubits in a subsystem. In this study, we employ quantum mutual information and the entanglement of formation (detailed discussion can be found in Appendix C) — both of which have well-defined expressions in the two-qubit scenario—to discern correlation patterns, here we take real image 1 and BAS  $4 \times 4$  dataset for example, the correlation between different qubit pairs can be seen in Fig. 7.

Fig. 8 illustrates the effects of reducing the operator pool within our adaptive circuit learning framework. We define the reduction rate  $r$  as the threshold for selecting two-qubit operators based on their correlation relative to the maximum observed correlation in the system:

$$\mathcal{P}_r = \{G_{ij} \in \mathcal{P} \mid I(q_i, q_j) \geq r \cdot I_{\max}\} \cup \{G_i \in \mathcal{P}\}, \quad (10)$$

$$I_{\max} = \max_{ij} I(q_i, q_j), \quad (11)$$





**FIG. 7:** Quantum mutual information and entanglement of formation for two different datasets. The axes correspond to qubit indices, and the correlation is evaluated on two-qubit subsystems of the target state  $|\Psi^*\rangle$  in Eq. (2). The color scale indicates the strength of the correlation, with brighter colors denoting stronger correlations and darker colors indicating weaker ones. Panel (a) shows the entanglement correlation for a real image dataset, where both quantum mutual information and entanglement of formation identify pairs of qubits with strong correlations. Quantum mutual information generally indicates a smoother transition than entanglement of formation. Panel (b) displays the entanglement correlation for the BAS  $4 \times 4$  dataset. Here, only quantum mutual information reflects the two-qubit correlation, whereas entanglement of formation registers zero correlation, suggesting that the BAS dataset may exhibit long-range entanglement, rendering two-qubit subsystem entanglement of formation immeasurable.

where  $\mathcal{P}_r$  represents the reduced operator pool,  $\mathcal{P}$  denotes the original full pool, and  $I(q_i, q_j)$  is the quantum mutual information between qubits indexed  $i$  and  $j$ . Here,  $G_{ij}$  symbolizes the two-qubit gates and  $G_i$  the single-qubit gates. This methodical reduction of the operator pool aims to retain only the most impactful gates, thereby streamlining the learning process while preserving the ability to capture essential quantum correlations. Fig. 8a presents experiments with reduction rates rang-

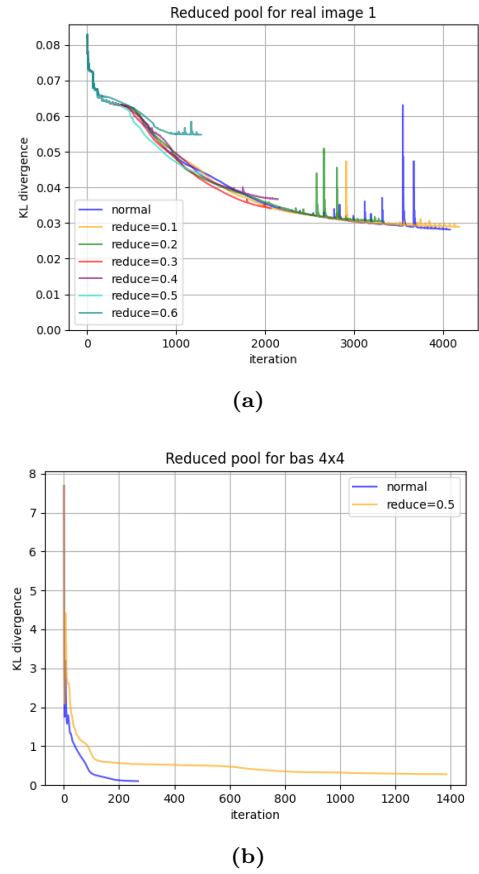


**FIG. 8:** Effect of operator pool reduction for different datasets. (a) For the real image 1 dataset, reduction rates from 0 to 0.6 were tested. Results indicate that reduction rates between 0.1 to 0.3 do not significantly impact the convergence of KL divergence. However, higher reduction rates result in a faster performance deterioration. (b) For the BAS  $4 \times 4$  dataset, a reduction rate of 0.5 was selected based on the sharp transition in mutual information observed in Fig. 7, targeting qubit pairs with strong correlations. Post-reduction, the reduced number of operators with significant gradients decrease  $N_o$  from 300 to 175. This adjustment led to a requirement for more iterations to achieve convergence and a slight decrease in performance.

ing from 0 to 0.6 for the real image 1 dataset. We observe that reduction rates up to 0.3 do not adversely affect the convergence of KL divergence, implying that moderate operator pruning is viable without significantly deteriorating the algorithm's performance. However, higher reduction rates result in a rapid decline in effectiveness.

For the BAS  $4 \times 4$  dataset, shown in Fig. 8b, we observe a stark transition in quantum mutual information. Consequently, we implemented a reduction rate of 0.5 to pinpoint operator pairs with heightened correlations. This selection, although it narrows the pool of operators, necessitates increasing  $N_o$  to 175, reflecting a strategic adjustment to a smaller set of operators with stronger gradients. Despite this modification, the algorithm

demands a greater number of iterations to achieve convergence, with a marginal reduction in performance. These results elucidate the nuanced advantages and potential drawbacks of reducing the operator pool and accentuate the importance of strategic operator selection informed by quantum correlation metrics to sustain algorithmic performance.

#### IV. CONCLUSIONS

In this work, we have introduced an adaptive circuit learning algorithm inspired by the ADAPT-VQE methodology, extending its principles to address the challenges of quantum data loading. Our innovative approach has demonstrated exceptional adaptability and robustness across a variety of datasets, including generic probability distributions, the Bars and Stripes (BAS) patterns, and real-world image data, showcasing significant improvements over existing methods.

Specifically, our algorithm’s ability to capture the intricate correlations present in image data using amplitude embedding has proven to be particularly effective. We have shown that it not only achieves superior performance in terms of convergence and precision but also overcomes the limitations typically associated with the entanglement range in other models. Moreover, our results highlight the critical importance of choosing an adequate number of operators and a dynamic learning rate to ensure the algorithm’s efficiency and accuracy.

The challenges encountered with QGAN [27] and QCBM [28] in larger problem sizes emphasize the need for careful hyperparameter selection and the design of circuit architectures that can cope with the complexity of the data involved. Our findings also suggest that while the MMD loss function is suitable for smaller datasets, it may not be the best fit for larger or more complex distributions, as seen with real image datasets.

Looking ahead, our study opens up several avenues for future exploration. One area of particular interest is the refinement of the adaptive circuit learning framework to further optimize parameter efficiency and convergence rates. Another promising direction is the investigation of different loss functions and their impact on the model’s

ability to approximate complex distributions more accurately. Additionally, our work offers compelling evidence that certain highly structured quantum states, which are characterized by a limited number of parameters, can be efficiently prepared using a relatively small number of gates. This raises the intriguing question of whether there is a deterministic algorithm that can directly acquire the gates to prepare these states, instead of relying on an adaptive method to select them. It is also currently unknown what precision of amplitude embedding is necessary for the approximation to be meaningful. Is a very precise quantum state required, or are states that capture the most critical features sufficient? We expect that further theoretical work is required to answer these questions.

As quantum computing continues to advance, the algorithms and techniques developed for quantum data loading will play a crucial role in harnessing the full potential of quantum resources. Our work represents a significant step toward achieving this goal, providing a robust foundation for future research in the field of quantum machine learning.

#### ACKNOWLEDGEMENTS

H.-C. Cheng is supported by the Young Scholar Fellowship (Einstein Program) of the Ministry of Science and Technology, Taiwan (R.O.C.) under Grants No. NSTC 111-2636-E-002-026, No. NSTC 112-2636-E-002-009, No. NSTC 112-2119-M-007-006, No. NSTC 112-2119-M-001-006, No. NSTC 112-2124-M-002-003, by the Yushan Young Scholar Program of the Ministry of Education, Taiwan (R.O.C.) under Grants No. NTU-111V1904-3, No. NTU-112V1904-4, and by the research project “Pioneering Research in Forefront Quantum Computing, Learning and Engineering” of National Taiwan University under Grant No. NTC-CC-112L893405. H.-C. Cheng acknowledges support from the “Center for Advanced Computing and Imaging in Biomedicine (NTU-112L900702)” through the Featured Areas Research Center Program within the framework of the Higher Education Sprout Project by the Ministry of Education (MOE) in Taiwan.

- 
- [1] A. W. Harrow, A. Hassidim, and S. Lloyd, *Physical review letters* **103**, 150502 (2009).
  - [2] A. M. Childs, *Nature Physics* **5**, 861 (2009).
  - [3] B. D. Clader, B. C. Jacobs, and C. R. Sprouse, *Physical review letters* **110**, 250504 (2013).
  - [4] S. Lloyd, M. Mohseni, and P. Rebentrost, *arXiv preprint arXiv:1307.0411* (2013).
  - [5] A. M. Childs and N. Wiebe, *arXiv preprint arXiv:1202.5822* (2012).
  - [6] D. W. Berry, A. M. Childs, R. Cleve, R. Kothari, and R. D. Somma, *Physical review letters* **114**, 090502 (2015).
  - [7] D. W. Berry, A. M. Childs, and R. Kothari, in *2015 IEEE 56th annual symposium on foundations of computer science (IEEE, 2015)* pp. 792–809.
  - [8] G. H. Low and I. L. Chuang, *Physical review letters* **118**, 010501 (2017).
  - [9] G. H. Low and I. L. Chuang, *Quantum* **3**, 163 (2019).
  - [10] A. Gilyén, Y. Su, G. H. Low, and N. Wiebe, in *Proceedings of the 51st Annual ACM SIGACT Symposium on*

- Theory of Computing* (2019) pp. 193–204.
- [11] E. Farhi, J. Goldstone, and S. Gutmann, arXiv preprint arXiv:1411.4028 (2014).
- [12] L. Zhou, S.-T. Wang, S. Choi, H. Pichler, and M. D. Lukin, *Physical Review X* **10**, 021067 (2020).
- [13] S. Hadfield, Z. Wang, B. O’gorman, E. G. Rieffel, D. Venturelli, and R. Biswas, *Algorithms* **12**, 34 (2019).
- [14] A. M. Childs, R. Cleve, E. Deotto, E. Farhi, S. Gutmann, and D. A. Spielman, in *Proceedings of the thirty-fifth annual ACM symposium on Theory of computing* (2003) pp. 59–68.
- [15] F. Magniez, M. Santha, and M. Szegedy, *SIAM Journal on Computing* **37**, 413 (2007).
- [16] S. Lloyd, M. Mohseni, and P. Rebentrost, *Nature Physics* **10**, 631 (2014).
- [17] P. Rebentrost, M. Mohseni, and S. Lloyd, *Physical review letters* **113**, 130503 (2014).
- [18] A. Barenco, C. H. Bennett, R. Cleve, D. P. DiVincenzo, N. Margolus, P. Shor, T. Sleator, J. A. Smolin, and H. Weinfurter, *Physical review A* **52**, 3457 (1995).
- [19] J. J. Vartiainen, M. Möttönen, and M. M. Salomaa, *Physical review letters* **92**, 177902 (2004).
- [20] V. V. Shende, S. S. Bullock, and I. L. Markov, in *Proceedings of the 2005 Asia and South Pacific Design Automation Conference* (2005) pp. 272–275.
- [21] M. Plesch and Č. Brukner, *Physical Review A* **83**, 032302 (2011).
- [22] X. Sun, G. Tian, S. Yang, P. Yuan, and S. Zhang, *IEEE Transactions on Computer-Aided Design of Integrated Circuits and Systems* (2023).
- [23] G. Rosenthal, arXiv preprint arXiv:2111.07992 (2021).
- [24] X.-M. Zhang, T. Li, and X. Yuan, *Physical Review Letters* **129**, 230504 (2022).
- [25] P.-L. Dallaire-Demers and N. Killoran, *Physical Review A* **98**, 012324 (2018).
- [26] S. Lloyd and C. Weedbrook, *Physical review letters* **121**, 040502 (2018).
- [27] C. Zoufal, A. Lucchi, and S. Woerner, *npj Quantum Information* **5**, 103 (2019).
- [28] J.-G. Liu and L. Wang, *Physical Review A* **98**, 062324 (2018).
- [29] C. Chow and C. Liu, *IEEE transactions on Information Theory* **14**, 462 (1968).
- [30] M. Benedetti, D. Garcia-Pintos, O. Perdomo, V. Leyton-Ortega, Y. Nam, and A. Perdomo-Ortiz, *npj Quantum Information* **5**, 45 (2019).
- [31] A. Kandala, A. Mezzacapo, K. Temme, M. Takita, M. Brink, J. M. Chow, and J. M. Gambetta, *nature* **549**, 242 (2017).
- [32] J. R. McClean, S. Boixo, V. N. Smelyanskiy, R. Babbush, and H. Neven, *Nature communications* **9**, 4812 (2018).
- [33] H. R. Grimsley, S. E. Economou, E. Barnes, and N. J. Mayhall, *Nature communications* **10**, 3007 (2019).
- [34] H. L. Tang, V. Shkolnikov, G. S. Barron, H. R. Grimsley, N. J. Mayhall, E. Barnes, and S. E. Economou, *PRX Quantum* **2**, 020310 (2021).
- [35] A. G. Taube and R. J. Bartlett, *International journal of quantum chemistry* **106**, 3393 (2006).
- [36] J. Romero, R. Babbush, J. R. McClean, C. Hempel, P. J. Love, and A. Aspuru-Guzik, *Quantum Science and Technology* **4**, 014008 (2018).
- [37] J. Lee, W. J. Huggins, M. Head-Gordon, and K. B. Whaley, *Journal of chemical theory and computation* **15**, 311 (2018).
- [38] M. Bilkis, M. Cerezo, G. Verdon, P. J. Coles, and L. Cincio, arXiv preprint arXiv:2103.06712 (2021).
- [39] L. Cincio, Y. Subaşı, A. T. Sornborger, and P. J. Coles, *New Journal of Physics* **20**, 113022 (2018).
- [40] L. Cincio, K. Rudinger, M. Sarovar, and P. J. Coles, *PRX Quantum* **2**, 010324 (2021).
- [41] K. Mitarai, M. Negoro, M. Kitagawa, and K. Fujii, *Physical Review A* **98**, 032309 (2018).
- [42] M. Schuld, V. Bergholm, C. Gogolin, J. Izaac, and N. Killoran, *Physical Review A* **99**, 032331 (2019).
- [43] D. P. Kingma and J. Ba, arXiv preprint arXiv:1412.6980 (2014).
- [44] V. Bergholm, J. Izaac, M. Schuld, C. Gogolin, S. Ahmed, V. Ajith, M. S. Alam, G. Alonso-Linaje, B. AkashNarayanan, A. Asadi, *et al.*, arXiv preprint arXiv:1811.04968 (2018).
- [45] A. Paszke, S. Gross, F. Massa, A. Lerer, J. Bradbury, G. Chanan, T. Killeen, Z. Lin, N. Gimelshein, L. Antiga, *et al.*, *Advances in neural information processing systems* **32** (2019).
- [46] D. J. MacKay, *Information theory, inference and learning algorithms* (Cambridge university press, 2003).
- [47] Z.-Y. Han, J. Wang, H. Fan, L. Wang, and P. Zhang, *Physical Review X* **8**, 031012 (2018).
- [48] W. K. Wootters, *Physical Review Letters* **80**, 2245 (1998).
- [49] W. K. Wootters, *Quantum Inf. Comput.* **1**, 27 (2001).

## Appendix A: Gradient evaluation

We illustrate that the gradient of a parameter can be explicitly computed with parameters-shift rule [41, 42], requiring three quantum circuit evaluations for each parameter. The derivative of the loss function  $\mathcal{L}(\boldsymbol{\theta})$  with respect to a specific parameter  $\theta_i$  is given by:

$$\frac{\partial \mathcal{L}(\boldsymbol{\theta})}{\partial \theta_i} = - \sum_x \frac{p(x)}{q_{\boldsymbol{\theta}}(x)} \frac{\partial q_{\boldsymbol{\theta}}(x)}{\partial \theta_i}, \quad (\text{A1})$$

where we introduce the following operators:

$$\begin{aligned} \Pi_x(\boldsymbol{\theta}) &\equiv U_{\ell}^{\dagger}(\theta_{\ell}) \dots U_{i+1}^{\dagger}(\theta_{i+1}) |x\rangle \langle x| U_{i+1}(\theta_{i+1}) \dots U_{\ell}(\theta_{\ell}) \\ \rho(\boldsymbol{\theta}) &\equiv U_{i-1}(\theta_{i-1}) \dots U_1(\theta_1) |0\rangle \langle 0| U_1^{\dagger}(\theta_1) \dots U_{i-1}^{\dagger}(\theta_{i-1}). \end{aligned} \quad (\text{A2})$$

The derivative of  $q_{\theta}(x)$  with respect to  $\theta_i$  can be expanded as

$$\begin{aligned}
\frac{\partial q_{\theta}(x)}{\partial \theta_i} &= \text{Tr} \left( \Pi_x(\boldsymbol{\theta}) \frac{\partial}{\partial \theta_i} \left[ U_i(\theta_i) \rho(\boldsymbol{\theta}) U_i^\dagger(\theta_i) \right] \right) \\
&= -\frac{i}{2} \text{Tr} \left( \Pi_x(\boldsymbol{\theta}) U_i(\theta_i) [P_i, \rho(\boldsymbol{\theta})] U_i^\dagger(\theta_i) \right) \\
&= \text{Tr} \left( \Pi_x(\boldsymbol{\theta}) U_i \left( \theta_i + \frac{\pi}{2} \right) \rho(\boldsymbol{\theta}) U_i^\dagger \left( \theta_i + \frac{\pi}{2} \right) \right) - \text{Tr} \left( \Pi_x(\boldsymbol{\theta}) U_i \left( \theta_i - \frac{\pi}{2} \right) \rho(\boldsymbol{\theta}) U_i^\dagger \left( \theta_i - \frac{\pi}{2} \right) \right) \\
&= q_{\theta + \frac{\pi}{2} \mathbf{e}_i}(x) - q_{\theta - \frac{\pi}{2} \mathbf{e}_i}(x).
\end{aligned} \tag{A3}$$

Thus, the gradient formula can be compactly expressed as:

$$\frac{\partial \mathcal{L}(\boldsymbol{\theta})}{\partial \theta_i} = - \sum_x \frac{p(x)}{q_{\theta}(x)} (q_{\theta + \frac{\pi}{2} \mathbf{e}_i}(x) - q_{\theta - \frac{\pi}{2} \mathbf{e}_i}(x)). \tag{A4}$$

This procedure simplifies the gradient evaluation to a series of tractable quantum measurements.

### Appendix B: Zero gradient operators

We establish that gradients vanish when initiating from a quantum state with solely real amplitudes and applying operators generated by an even number of Pauli  $Y$  operators. This phenomenon can be inspected as follows: Introducing an operator into a circuit yields

$$\begin{aligned}
\frac{\partial q_{\theta}(x)}{\partial \theta_i} &= \text{Tr} \left( |x\rangle\langle x| \frac{\partial}{\partial \theta_i} \left[ U_i(\theta_i) \rho(\boldsymbol{\theta}) U_i^\dagger(\theta_i) \right] \right) \Bigg|_{\theta_i=0} \\
&= -\frac{i}{2} \text{Tr} (|x\rangle\langle x| [P_i, \rho(\boldsymbol{\theta})]) \\
&= -\frac{i}{2} (\langle x| P_i \rho(\boldsymbol{\theta}) |x\rangle - \langle x| \rho(\boldsymbol{\theta}) P_i |x\rangle) \\
&= -\frac{i}{2} (\langle x| P_i \rho(\boldsymbol{\theta}) |x\rangle - \langle x| P_i \rho(\boldsymbol{\theta}) |x\rangle^*) \\
&= 0,
\end{aligned} \tag{B1}$$

where the last equality is deduced from the initial state  $\rho(\boldsymbol{\theta})$  and the generator  $P_i$  being real. Consequently, the absence of imaginary components results in a zero gradient due to the real nature of the elements involved.

### Appendix C: Quantum Mutual Information and Entanglement of Formation

Quantum mutual information (QMI) is a measure of the total correlation between two subsystems of a quantum state. It quantifies not only classical correlations but also encompasses quantum entanglement, providing a complete picture of the correlations present in a quantum system. The QMI of a bipartite state  $\rho_{AB}$  is defined as:

$$I(A : B) = S(\rho_A) + S(\rho_B) - S(\rho_{AB}), \tag{C1}$$

where  $S(\rho)$  denotes the von Neumann entropy of the state  $\rho$ , and  $\rho_A$  and  $\rho_B$  are the reduced density matrices of subsystems A and B, respectively.

Entanglement of formation (EOF) [48, 49] is a conceptually distinct measure that specifically quantifies the resources needed to create a given entangled state. For a bipartite quantum state  $\rho_{AB}$ , the EOF is the minimum average entanglement of an ensemble of pure states that represents  $\rho_{AB}$ . Formally, if  $\rho_{AB} = \sum_i p_i |\psi_i\rangle\langle\psi_i|$ , where  $|\psi_i\rangle$  are pure states and  $p_i$  are the probabilities of the states, the EOF is given by:

$$E_F(A : B) = \min \sum_i p_i E(|\psi_i\rangle), \tag{C2}$$

where  $E(|\psi_i\rangle)$  is the entanglement entropy of the state  $|\psi_i\rangle$ .

For two-qubit systems, EOF has a closed-form expression, which is derived from the measure known as concurrence. The concurrence,  $C$ , for a pair of qubits in a mixed state  $\rho$ , is calculated as:

$$C(\rho) = \max\{0, \lambda_1 - \lambda_2 - \lambda_3 - \lambda_4\}, \quad (\text{C3})$$

where  $\lambda_i$  (for  $i = 1, 2, 3, 4$ ) are the square roots of the eigenvalues, in descending order, of the non-Hermitian matrix  $\rho\tilde{\rho}$ . Here,  $\tilde{\rho}$  is the spin-flipped state of  $\rho$ :

$$\tilde{\rho} = (\sigma_y \otimes \sigma_y)\rho^*(\sigma_y \otimes \sigma_y), \quad (\text{C4})$$

and  $\rho^*$  denotes the complex conjugate of  $\rho$  in a fixed basis such as  $\{|00\rangle, |01\rangle, |10\rangle, |11\rangle\}$ .

The EOF can then be expressed as a function of concurrence:

$$E_F(\rho) = h\left(\frac{1 + \sqrt{1 - C(\rho)^2}}{2}\right), \quad (\text{C5})$$

where  $h(x) = -x \log_2 x - (1 - x) \log_2(1 - x)$  represents the binary entropy function.

This relationship provides a direct method to calculate EOF from the density matrix of two-qubit states, offering a valuable tool for quantifying entanglement.

In the case of partitioned systems, where we focus on a two-qubit subsystem  $A, B$  within a larger system that includes  $C$ , the bipartite state  $\rho_{AB}$  can be obtained by tracing out subsystem  $C$ :

$$\rho_{AB} = \text{Tr}_C(\rho_{ABC}). \quad (\text{C6})$$

## Appendix D: Experiment results

Experiment results				
Datasets	QGAN	QCBM	DDQCL	ACLBM
log normal 3	$2.71 \times 10^{-2}$	$1.46 \times 10^{-10}$	$6.09 \times 10^{-7}$	$2.98 \times 10^{-6}$
	0.7206 / 0.6894	$2.88 \times 10^{-11}$	$6.09 \times 10^{-7}$	$2.98 \times 10^{-6}$
bimodal 3	$1.74 \times 10^{-2}$	$2.38 \times 10^{-8}$	$3.96 \times 10^{-7}$	$3.31 \times 10^{-6}$
	0.6994 / 0.6905	$1.47 \times 10^{-9}$	$3.96 \times 10^{-7}$	$3.31 \times 10^{-6}$
triangular 3	$1.12 \times 10^{-2}$	$2.84 \times 10^{-5}$	$2.94 \times 10^{-6}$	$1.66 \times 10^{-6}$
	0.6969 / 0.6926	$4.41 \times 10^{-7}$	$2.94 \times 10^{-6}$	$1.66 \times 10^{-6}$
log normal 10	$3.48 \times 10^{-1}$	$9.61 \times 10^{-2}$	$1.12 \times 10^{-1}$	$3.25 \times 10^{-4}$
	0.7571 / 0.6762	$6.41 \times 10^{-5}$	$1.12 \times 10^{-1}$	$3.25 \times 10^{-4}$
bimodal 10	$5.93 \times 10^{-1}$	$2.98 \times 10^{-1}$	$1.28 \times 10^{-1}$	$4.73 \times 10^{-4}$
	0.7746 / 0.6664	$2.10 \times 10^{-4}$	$1.28 \times 10^{-1}$	$4.73 \times 10^{-4}$
triangular 10	$5.45 \times 10^{-1}$	$3.29 \times 10^{-1}$	$1.31 \times 10^{-1}$	$5.00 \times 10^{-4}$
	0.7702 / 0.6670	$3.12 \times 10^{-4}$	$1.31 \times 10^{-1}$	$5.00 \times 10^{-4}$
bas 2x2	$1.49 \times 10^{-3}$	$1.68 \times 10^{-2}$	$1.48 \times 10^{-5}$	$1.81 \times 10^{-6}$
	0.6944 / 0.6927	$4.34 \times 10^{-5}$	$1.48 \times 10^{-5}$	$1.81 \times 10^{-6}$
bas 3x3	3.86	$2.30 \times 10^{-2}$	$2.63 \times 10^{-2}$	$6.36 \times 10^{-4}$
	0.6967 / 0.6905	$8.53 \times 10^{-5}$	$2.63 \times 10^{-2}$	$6.36 \times 10^{-4}$
bas 4x4	10.46	4.46	$1.54 \times 10^{-1}$	$1.03 \times 10^{-1}$
	$5.39 \times 10^{-3}$ / 13.0612	$5.58 \times 10^{-2}$	$1.52 \times 10^{-1}$	$1.03 \times 10^{-1}$
real image 1	12.73	$6.16 \times 10^{-1}$	$5.06 \times 10^{-1}$	$2.82 \times 10^{-2}$
	5.7377 / 13.8094	$4.58 \times 10^{-5}$	$5.06 \times 10^{-1}$	$2.82 \times 10^{-2}$
real image 2	13.81	$8.62 \times 10^{-1}$	$5.44 \times 10^{-1}$	$4.22 \times 10^{-2}$
	8.8076 / 13.8156	$1.67 \times 10^{-3}$	$5.44 \times 10^{-1}$	$4.22 \times 10^{-2}$
real image 3	11.85	$5.70 \times 10^{-1}$	$4.98 \times 10^{-1}$	$1.62 \times 10^{-2}$
	4.7950 / 13.7895	$2.56 \times 10^{-5}$	$4.98 \times 10^{-1}$	$1.62 \times 10^{-2}$

**TABLE I:** Experimental results across various datasets and benchmark models. Each row is divided into two subrows: the upper subrow displays the KL divergence, while the lower subrow presents the specific loss metric employed by each model. For QGAN, the loss is associated with the generator and discriminator; for QCBM, it is the MMD loss; and for DDQCL and ACLBM, it is the KL divergence.